

Physical validation of simulators in Computer Graphics: Supplementary Document

VICTOR ROMERO, Univ. Grenoble Alpes, Inria, CNRS, Grenoble INP, LJK, France

MICKAËL LY, Univ. Grenoble Alpes, Inria, CNRS, Grenoble INP, LJK, France

ABDULLAH-HAROON RASHEED, Univ. Grenoble Alpes, Inria, CNRS, Grenoble INP, LJK, France

RAPHAËL CHARRONDIÈRE, Univ. Grenoble Alpes, Inria, CNRS, Grenoble INP, LJK, France

ARNAUD LAZARUS, Sorbonne Université, CNRS, Institut Jean Le Rond d'Alembert, UMR 7190, France

SÉBASTIEN NEUKIRCH, Sorbonne Université, CNRS, Institut Jean Le Rond d'Alembert, UMR 7190, France

FLORENCE BERTAILS-DESCOUBES, Univ. Grenoble Alpes, Inria, CNRS, Grenoble INP, LJK, France

ACM Reference Format:

Victor Romero, Mickaël Ly, Abdullah-Haroon Rasheed, Raphaël Charrondière, Arnaud Lazarus, Sébastien Neukirch, and Florence Bertails-Descoubes. 2021. Physical validation of simulators in Computer Graphics: Supplementary Document. *ACM Trans. Graph.* 40, 4, Article 66 (August 2021), 16 pages. <https://doi.org/10.1145/3450626.3459931>

INTRODUCTION

We group here some additional material not included in the main text of *Physical validation of simulators in Computer Graphics: A new framework dedicated to slender elastic structures and frictional contact*, refereed to as 'the Paper' in the following. The present document comprises six sections. In Section 1 we present convergence studies for the different codes used in the four protocols introduced in the Paper. In Section 2, we show some of the meshes used in the study, and in Section 3 we give details on the input parameters for ARCSIM and LIBSHELL. In Section 4, we present in detail our protocols for experimental validation. In Section 5 we present the numerical and experimental results for a setup derived from the **Lateral Buckling** test. In Section 6 we list all the numerical plots on the **Cantilever** test as some of these could not be included in the Paper, due to space limitation. Finally in Section 7 we give some additional information on the codes used in the present study.

CONTENTS

Contents	1
1 Convergence studies	1
1.1 Convergence results for the Cantilever test	2
1.2 Convergence results for the Bend-Twist test	5
1.3 Convergence results for the Lateral Buckling test	6
1.4 Convergence results for the Stick-Slip test	9
2 Some of the meshes used	10
3 Input parameters for ARCSIM and LIBSHELL	11
3.1 Bending formulas	11
3.2 Input format	11
4 Experimental protocols	12
4.1 Materials	12
4.2 Experimental setups	12
5 Rotation experiment behind the Lateral Buckling test	14
5.1 Description	14
5.2 Results and analysis	14
6 Full results on the Cantilever test	15
7 Some more information on the codes used	16
References	16

Authors' addresses: Victor Romero, Univ. Grenoble Alpes, Inria, CNRS, Grenoble INP, LJK, 38000, Grenoble, France, victor.romero@inria.fr; Mickaël Ly, Univ. Grenoble Alpes, Inria, CNRS, Grenoble INP, LJK, 38000, Grenoble, France, mickael.ly@inria.fr; Abdullah-Haroon Rasheed, Univ. Grenoble Alpes, Inria, CNRS, Grenoble INP, LJK, 38000, Grenoble, France, haroon.rasheed@inria.fr; Raphaël Charrondière, Univ. Grenoble Alpes, Inria, CNRS, Grenoble INP, LJK, 38000, Grenoble, France, raphael.charrondiere@inria.fr; Arnaud Lazarus, Sorbonne Université, CNRS, Institut Jean Le Rond d'Alembert, UMR 7190, 4 place Jussieu, case 162, F-75005, Paris, France, arnaud.lazarus@upmc.fr; Sébastien Neukirch, Sorbonne Université, CNRS, Institut Jean Le Rond d'Alembert, UMR 7190, 4 place Jussieu, case 162, F-75005, Paris, France, sebastien.neukirch@upmc.fr; Florence Bertails-Descoubes, Univ. Grenoble Alpes, Inria, CNRS, Grenoble INP, LJK, 38000, Grenoble, France, florence.descoubes@inria.fr.

Publication rights licensed to ACM. ACM acknowledges that this contribution was authored or co-authored by an employee, contractor or affiliate of a national government. As such, the Government retains a nonexclusive, royalty-free right to publish or reproduce this article, or to allow others to do so, for Government purposes only.

© 2021 Copyright held by the owner/author(s). Publication rights licensed to the Association for Computing Machinery.

0730-0301/2021/8-ART66 \$15.00

<https://doi.org/10.1145/3450626.3459931>

1 CONVERGENCE STUDIES

We show in this section the output of some of the codes tested in the Paper, but with different number of elements for the spatial discretisation of the structures.

Please note that computing times are given here as mere indications and should not be seen as benchmarking.

1.1 Convergence results for the **Cantilever** test

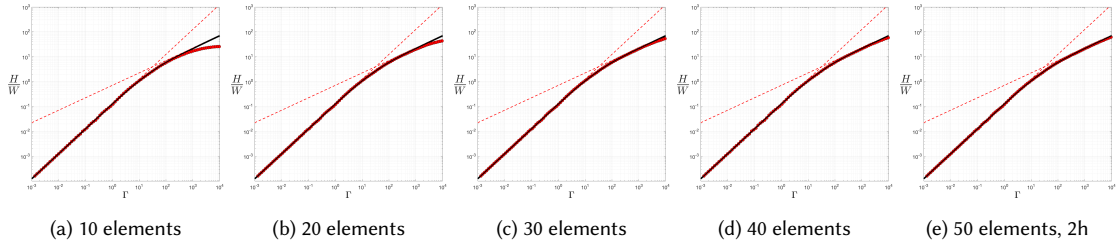


Fig. 1. Convergence results of SUPER-HELIX on the **Cantilever** test.

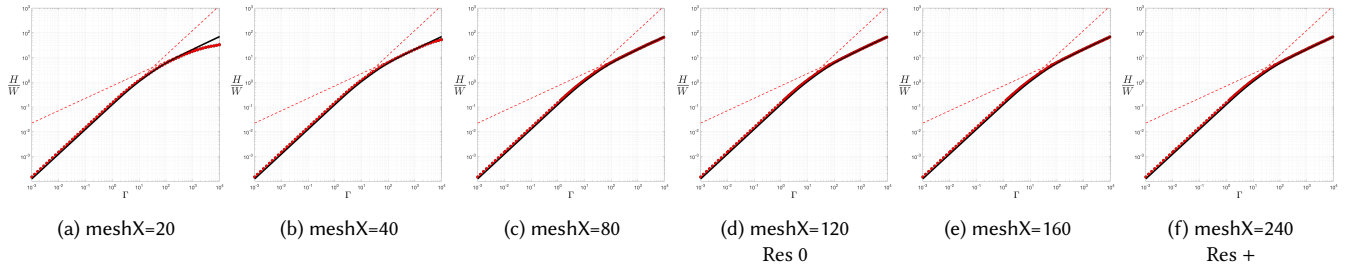


Fig. 2. Convergence results of FENICSHELL on the **Cantilever** test. The parameter meshX is the number of mesh points along L , the number mesh points along w being $\text{meshX} \times w/L$. The entire set of graphs was produced in about 1h.

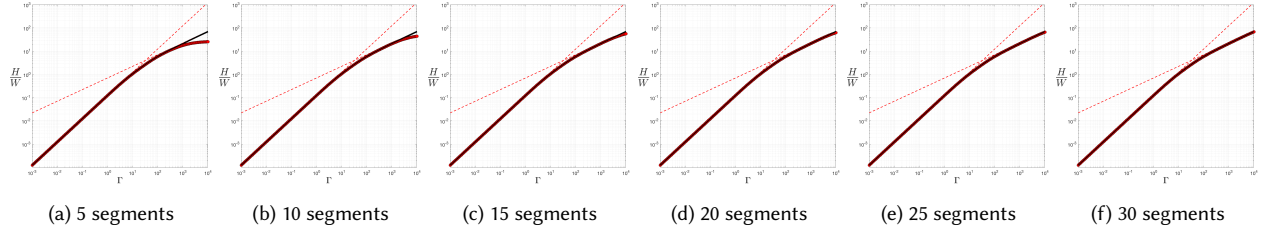


Fig. 3. Convergence results of SUPER-RIBBON on the **Cantilever** test. The entire set of graphs was produced in about 10 min.

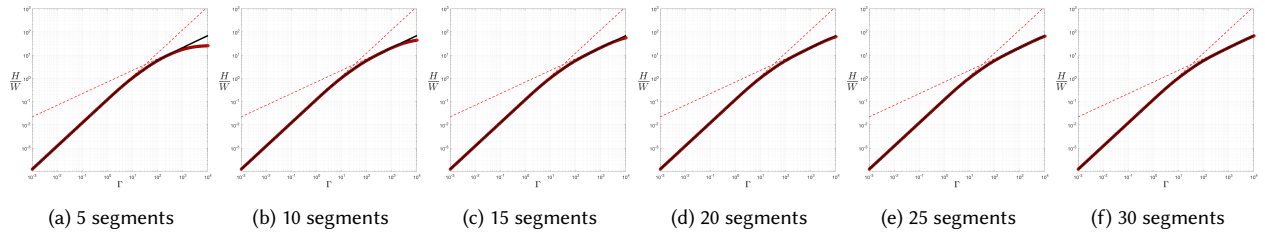


Fig. 4. Convergence results of SUPER-CLOTHOID on the **Cantilever** test. The entire set of graphs was produced in about 20 min.

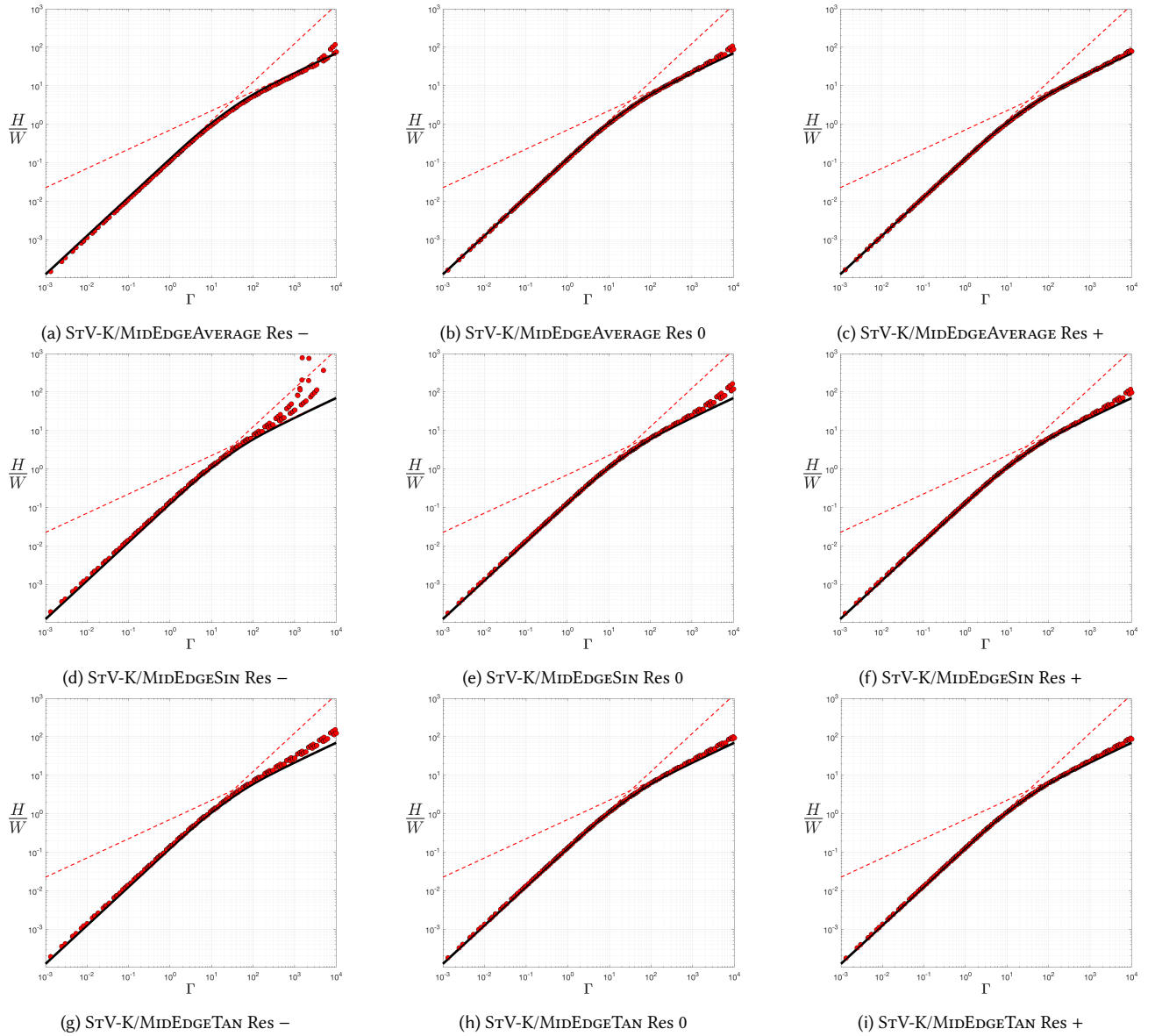


Fig. 5. Convergence results of LIBSHELL on the **Cantilever** test. Plots on the left column took about 10 min each, plots in the center column about 1 or 2h each, and plots in the right column about 8h each. For the **Cantilever** test, Res - has meshX=55, Res 0 has meshX=120, and Res + has meshX=240. The parameter meshX is the number of mesh points along L , the number mesh points along w being $\text{meshX} \times w/L$.

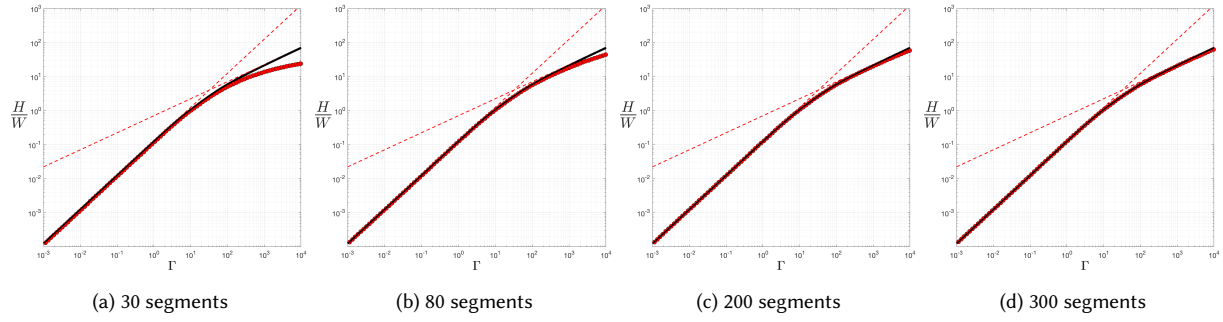


Fig. 6. Convergence results of DISCRETE ELASTIC ROD on the **Cantilever** test. The entire set of graphs was produced in about 3 days.

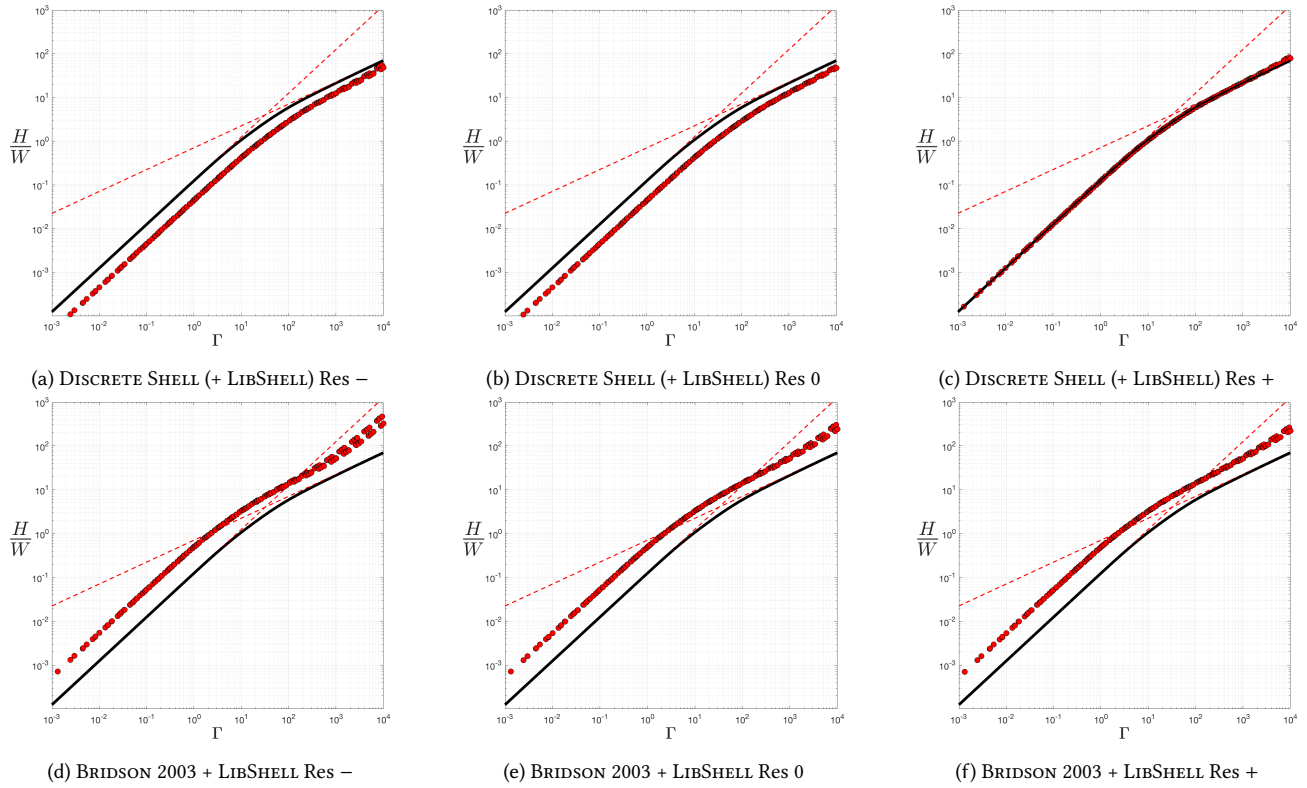


Fig. 7. Convergence results of the hinge models on the **Cantilever** test.

1.2 Convergence results for the **Bend-Twist** test

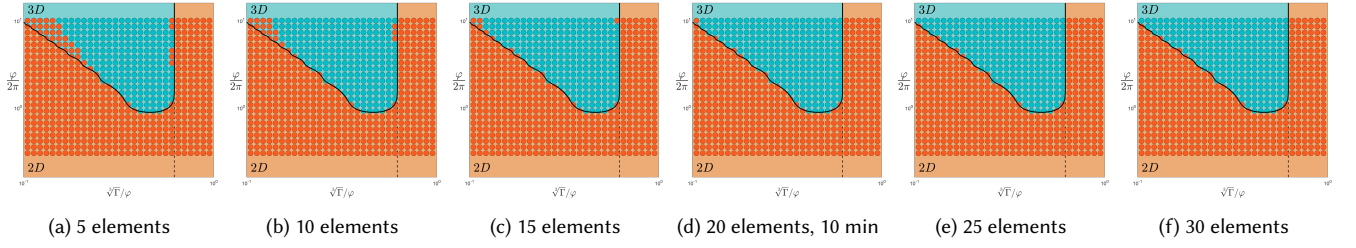


Fig. 8. Convergence results of SUPER-CLOTHOID on the **Bend-Twist** test. Approximate time for computing all these graphs: $\sim 1h$

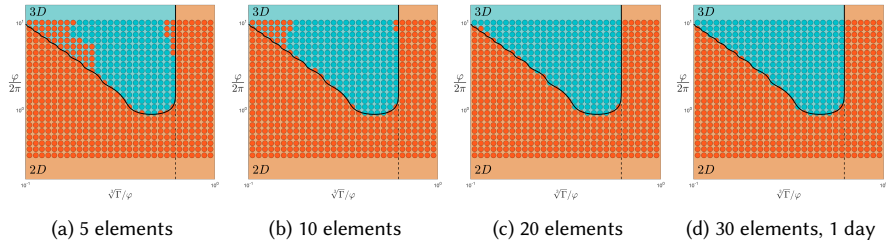


Fig. 9. Convergence results of SUPER-HELIX on the **Bend-Twist** test.

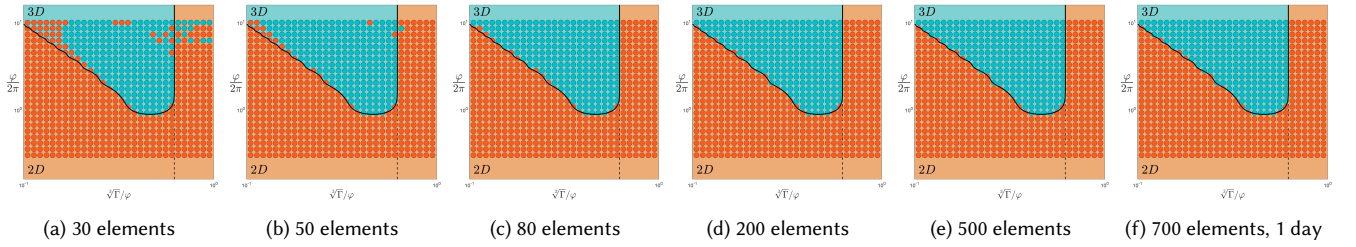


Fig. 10. Convergence results of DISCRETE ELASTIC ROD on the **Bend-Twist** test.

1.3 Convergence results for the **Lateral Buckling** test

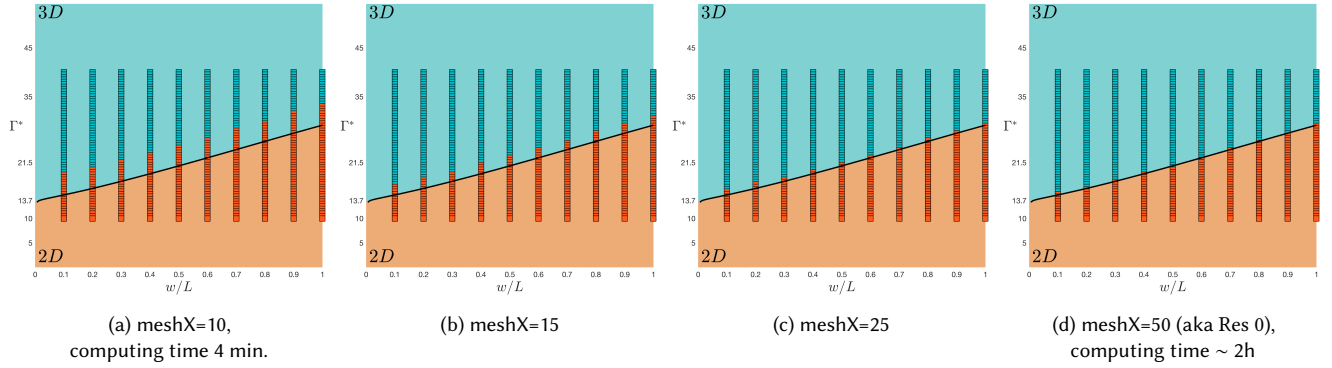


Fig. 11. Convergence results of FENICSSHELL on the **Lateral Buckling** test. The parameter meshX is the number of mesh points along L , the number mesh points along w being $\text{meshX} \times w/L$.

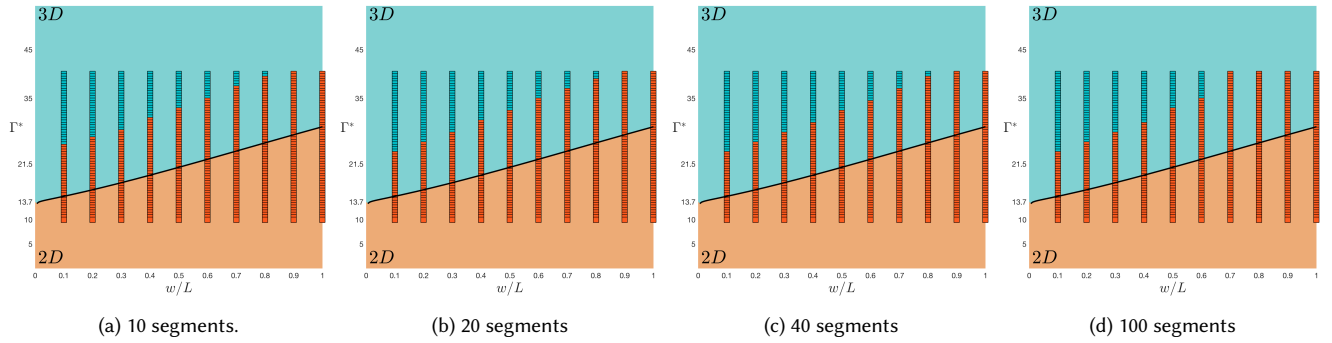


Fig. 12. Convergence results of WUNDERLICH CLAMPED on the **Lateral Buckling** test. This set of data took around 10 min to be generated.

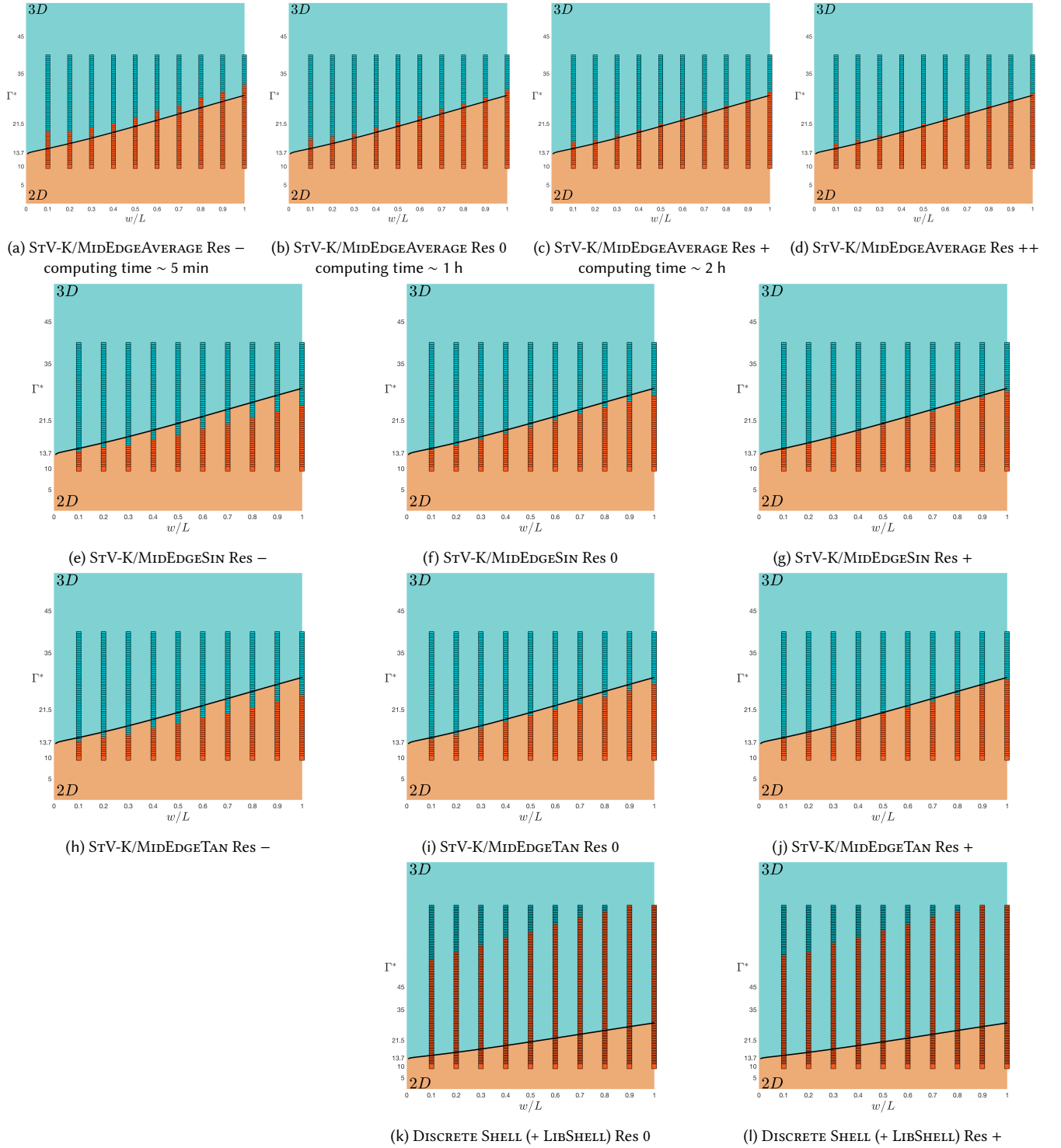


Fig. 13. Convergence results of LIBSHELL on the **Lateral Buckling** test. The parameter meshX is the number of mesh points along L , the number mesh points along w being $\text{meshX} \times w/L$. For the **Lateral Buckling** test, Res - has meshX=25, Res 0 has meshX=50, Res + has meshX=75, and Res ++ has meshX=100.

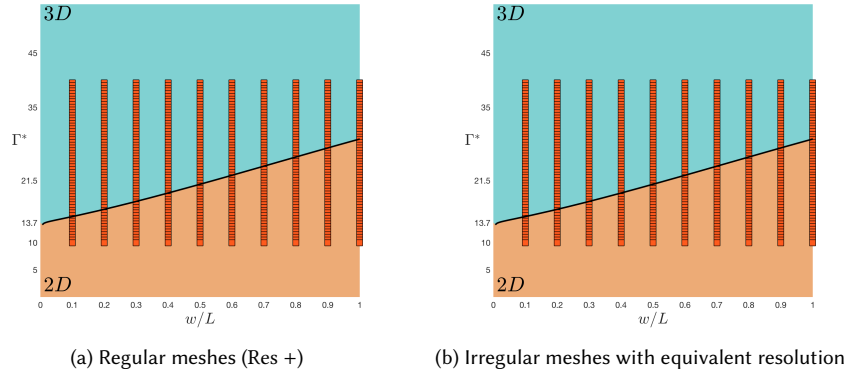


Fig. 14. Comparison of the results of the **Lateral Buckling** test on DISCRETE SHELL (+ LIBSHELL) with differently mesh inputs. We observed no notable difference between the regular and irregular mesh cases.

1.4 Convergence results for the **Stick-Slip** test

For ARGUS NON ADAPTIVE, BRIDSON-HARMON, and PROJECTIVE FRICTION, the fixed mesh had 350 vertices in total with 50 vertices along the length. The adaptive mesh for ARGUS was an empty mesh with just the corner points. All meshes were of length 0.2 m and width 0.01 m.

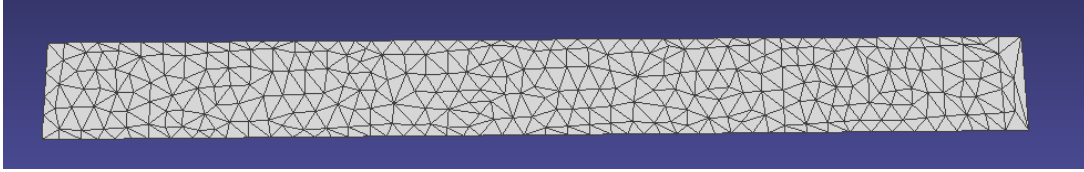


Fig. 15. Example mesh for the **Stick-Slip** test.

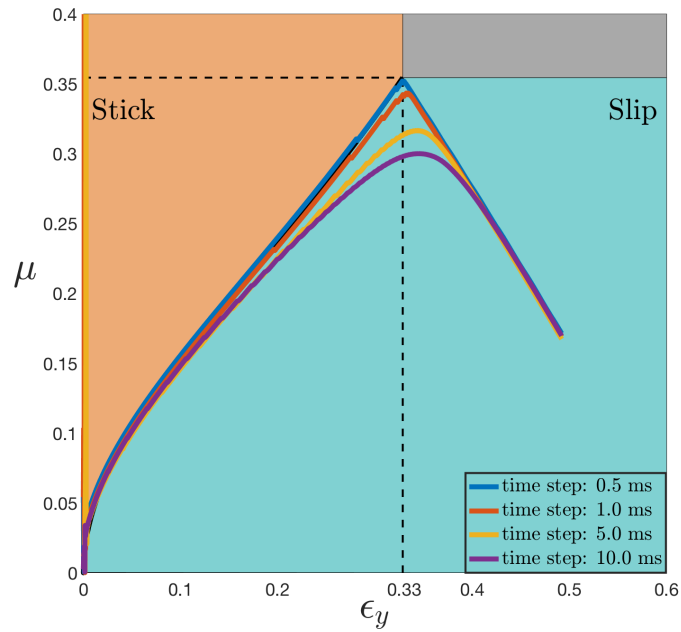


Fig. 16. Convergence study for the **Stick-Slip** test with the SO-BOGUS (+ SUPER-HELIX 2D) code. We show $\mu = Q/P$ for different values of the time step. As the time step is decreased, the total number of steps is increased in order to keep a total simulated duration of 60 sec. The coefficients for viscosity and internal friction are set to 10.

2 SOME OF THE MESHES USED

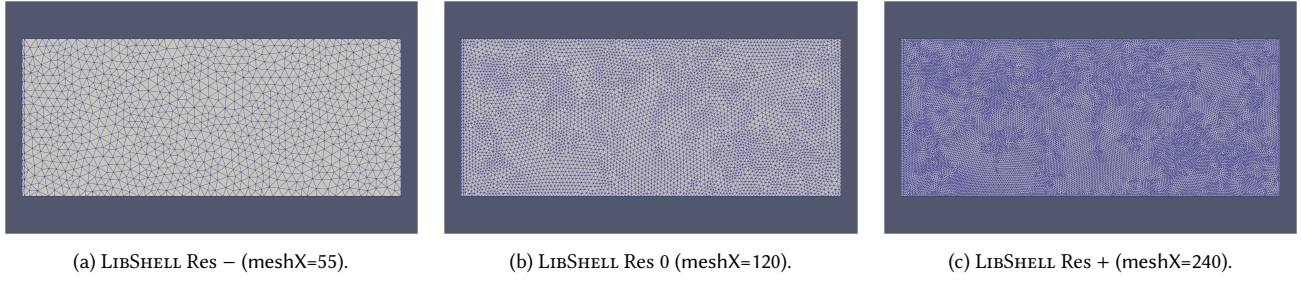


Fig. 17. Some of the meshes used on the **Cantilever** setup. The parameter meshX is the number of mesh points along L , the number mesh points along w being $\text{meshX} \times w/L$. Here $w/L = 0.4125$.

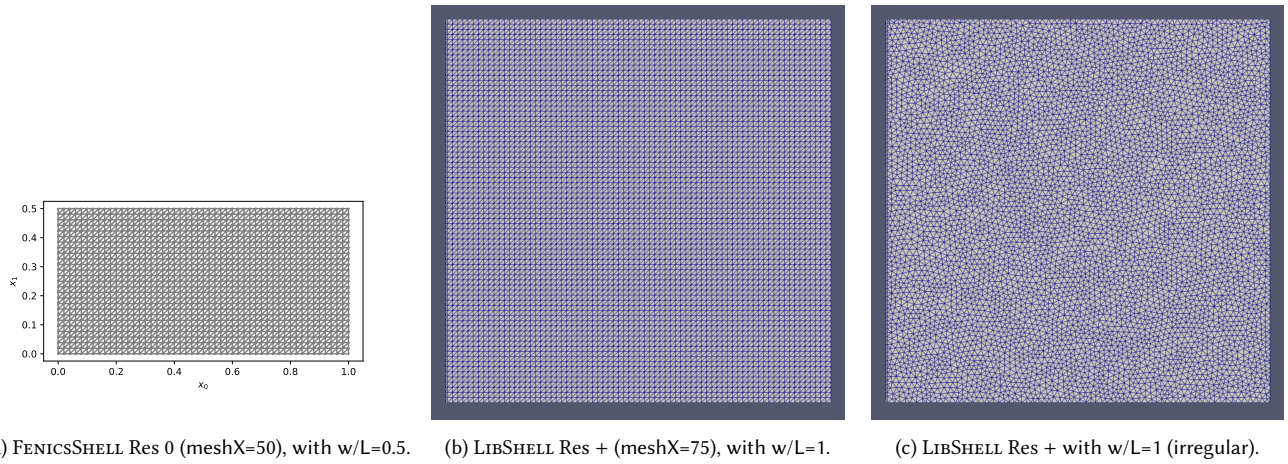


Fig. 18. Some of the meshes used on the **Lateral Buckling** setup. The parameter meshX is the number of mesh points along L , the number mesh points along w being $\text{meshX} \times w/L$.

3 INPUT PARAMETERS FOR ARCSIM AND LIBSHELL

3.1 Bending formulas

Hinge energy. We describe here the bending hinge energy for triangular meshes, introduced concurrently by Grinspun et al. [2003] and Bridson et al. [2003]. Both are based on the dihedral angle between two neighbouring faces noted θ (see inset Figure), weighted by a coefficient accounting for the mesh resolution. However, their formulations differ slightly, as Grinspun et al. [2003]'s formulation is

$$k_B \frac{3L^2}{A} (\theta - \bar{\theta})^2 \quad (1)$$

while Bridson et al. [2003] is

$$k_B \frac{L^2}{4A} (\sin(\theta) - \sin(\bar{\theta}))^2, \quad (2)$$

with $\bar{\theta}$ the angle at rest, L the length of the common edge, A_i the area of the face f_i , and $A = A_1 + A_2$. One may also use the equivalent formulation $\frac{L}{\frac{h_1+h_2}{2}}$ for the geometric coefficient, with h_i the height of the triangle f_i .

As mentioned in the Paper, these two formulations differ on two points. According to their discretization of a continuous energy, Grinspun et al. [2003] obtain their formula with a factor 3 and use directly the dihedral angles, while Bridson et al. [2003] obtain a factor $\frac{1}{4}$ from their heuristic and use the sines of the angles, which are easier to compute than the angles themselves.

Using the angle or its sine are equivalent for small deflections, and may only affect accuracy in the regime of high Γ values in our **Cantilever** experiment. However, note that we did not test the sin formulation since ARCSIM's original implementation actually directly relies on the dihedral angle θ and its derivative. Moreover, in the ARCSIM implementation, be mindful to note that an additional $\frac{1}{2}$ factor is present, leading to this *alternative* formula for Bridson et al. [2003]'s energy,

$$\frac{k_E}{2} \frac{L^2}{4A} (\theta - \bar{\theta})^2 \quad \text{with } k_E = 2k_B. \quad (3)$$

The main difference to us, when comparing (1) and (3) is thus the scaling coefficient of 12 between the two formulas, which yields a vertical shift between the two models, as shown in the Paper.

Discrete Koiter's shell energy. Described in [Chen et al. 2018], the discrete version of the Koiter's shell energy directly stems from the continuous formula where the first and second fundamental forms are replaced by their discrete equivalents on triangular meshes.

For the bending term, it leads to an energy defined per face that reads as

$$\frac{1}{2} \frac{h^3}{12} \|\bar{a}^{-1}(b - \bar{b})\|_{SV}^2 \sqrt{\det \bar{a}} \quad (4)$$

with h the thickness of the shell, a and b the first and second discrete fundamental forms defined on the triangular face and the bar quantities denoting the rest configurations. The norm $\|\bullet\|_{SV}^2$ is called

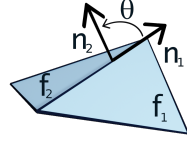


Fig. 19. Dihedral angle between two faces.

the "Saint-Venant-Kirchoff" norm, defined by

$$\|\bullet\|_{SV}^2 = \frac{\lambda}{2} \text{tr}(\bullet)^2 + \mu \text{tr}(\bullet^2) \quad (5)$$

with λ and μ the first and second 2D Lamé parameters defined as

$$\lambda = \frac{Ev}{1-\nu^2}; \mu = \frac{E}{2(1+\nu)} \quad (6)$$

with E the Young modulus and ν the Poisson ratio.

3.2 Input format

To test the physical accuracy of the codes, we must be able to compute bending coefficients from the physical parameters.

For LIBSHELL, we simply fill in the values for the geometry of the plate, the Young modulus and Poisson ratio. For DISCRETE SHELL and ARCSIM, we need to define the k_B parameter of the hinge energy. Following [Tamstorf and Grinspun 2013], we identify k_B with half the bending rigidity,

$$k_B = \frac{D}{2} = \frac{Eh^3}{24(1-\nu^2)} \quad (7)$$

which directly gives a good agreement on DISCRETE SHELL.

For ARCSIM, an extra step needs to be carried on to incorporate this bending modulus. Indeed, the implementation stems from Wang et al. [2011] who used an orthotropic "by part" model to approximate the anisotropic behavior of cloth. As such, in practice, the stretching and bending coefficients are interpolated between 5 set of fitted coefficients depending on the cloth orientation. Hence, to perform our test, the material input file needs to be composed of five times the same elasticity matrix and 5 times the same bending matrix.

For bending, as noted in Equation 3, a factor $\frac{1}{2}$ is already present, so the bending matrix we have to use to fill in the k_E value is

$$D \text{diag}(1, 1, 1). \quad (8)$$

For stretching, ARCSIM considers that cloth is a linear orthotropic material, i.e. a linear anisotropic material with 3 symmetry axes. It can thus be characterized by the following linear strain-stress relationship [Wang et al. 2011],

$$\sigma = \begin{bmatrix} \sigma_{uu} \\ \sigma_{vv} \\ \sigma_{uv} \end{bmatrix} = \begin{bmatrix} c_{11} & c_{12} & 0 \\ c_{12} & c_{22} & 0 \\ 0 & 0 & c_{33} \end{bmatrix} \begin{bmatrix} \varepsilon_{uu} \\ \varepsilon_{vv} \\ \varepsilon_{uv} \end{bmatrix} = C\varepsilon,$$

where σ is the (plate) stress tensor and ε the (plate) strain tensor.

Here we assume that the material is isotropic (Hookean material), meaning that the 4 coefficients c_{ij} are not independent, but given by the following formulas [Audoly and Pomeau 2010, Sec. 6.4]

$$\begin{cases} c_{11} = \frac{E}{1-\nu^2} \\ c_{12} = \frac{E\nu}{1-\nu^2} = \nu c_{11} \\ c_{22} = \frac{E}{1-\nu^2} = c_{11} \\ c_{33} = \frac{E}{1+\nu} \end{cases}$$

4 EXPERIMENTAL PROTOCOLS

4.1 Materials

Our four tests require rods, plates and ribbons with controlled geometry and known mechanical properties. Ribbons and plates are made by cutting rectangular pieces, with the desired dimensions, out of large plastic sheets. The most relevant characteristic is the flatness of the sample. The PRO Shim Kit by RS Components (RS Stock No.:770-816) was found to be the best for our purposes, see Figure 20. This set of plastic sheets are made out of polyethylene terephthalate, PET, which has a Young modulus in the order of 5 GPa and they come in thickness ranging from 50 to 500 μm . These values are only estimations and for our tests we characterize our samples mechanically and geometrically by ourselves.



Fig. 20. Samples of PET sheets used for our experimental tests.

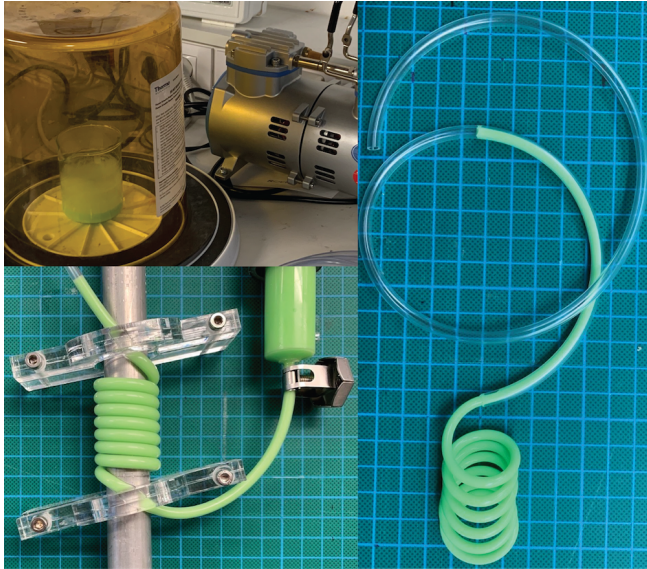


Fig. 21. **Fabrication process of an elastomeric model rod.** *Top left:* Degassing in a vacuum chamber. *Bottom left:* Polymer injection on coiled PVC tube. *Right:* Final shape of the rod after pulling out a large portion of rod from the PVC tube.

Curly and flat rods are fabricated using vinyl polysiloxane commercialised by Zhermack™. For our rods to have a Young's modulus in the order of 1 MPa, we use Elite32™. This product comes with a base and a curing catalyser that have to be scrupulously mixed in a 1:1 proportion. The mixing process produces accumulation of air in the mixture, therefore to achieve the expected elastic behaviour one needs to remove it while the mixture is fluid. To this end, we

degas the mixture by reducing pressure in a vacuum chamber for 2 minutes (see top left image in Figure 21). We observe that in this time most of the trapped air has been removed and the mixture remains fluid.

By means of a syringe, we inject the polymer into a PVC tube (see bottom left image in Figure 21). The final natural geometry of the moulded rod will be determined by the shape in which the PVC tube is arranged. Naturally curly rods are obtained by coiling the PVC tube around a metallic cylinder and holding it in a given configuration. For straight rods, we keep the PVC tube straight. Polymerisation takes about few hours, but to be on the safe side we usually let the polymer settle for 24 hours before removing it from the tube. Because silicon based polymers do not adhere to PVC, we simply pull the elastic rod out of the tube, see right image in Figure 21.

4.2 Experimental setups

The Cantilever setup, shown in Figure 26a, is a simple arrangement of a clamp held by two pillars where rods and ribbons are clamped tightly. The length of the sample is measured when it is placed on the clamp and we are careful to orthogonally align the sample to the clamp. To measure the deformation, we fix a graduated rail that allows vertical displacements of an horizontal metallic bar. For each sample length, we let the sample deflect and reach its equilibrium shape. We move the horizontal bar to the same height as the free end and measure H on the graduated vertical rail. Finally, W is measured with a ruler along the horizontal bar from the rail to the sample free-end. In Figure 22, we show the results for the measured aspect ratio as a function of the length for samples with different thickness, widths and made of different materials (VPS, Acetate and PET).

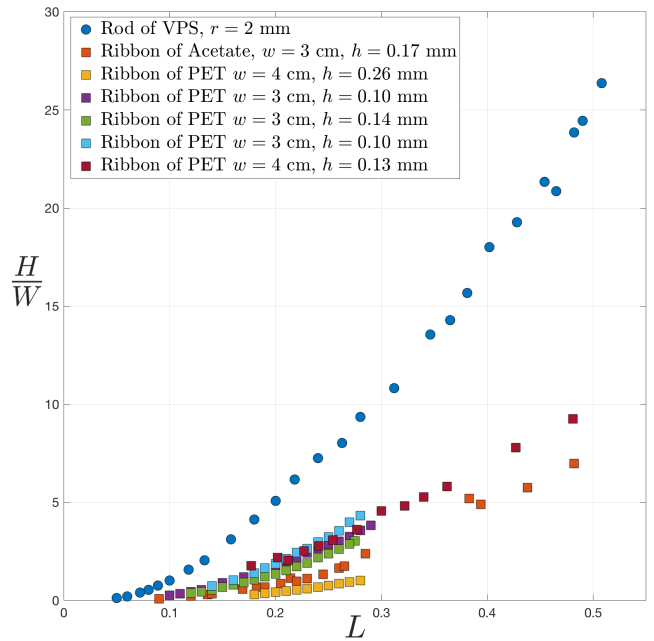


Fig. 22. Raw data **Cantilever test**

The **Bend-Twist** setup, shown in Figure 26b, is built only for illustration purposes since we rely on the experimental validation and the large data set presented in [Miller et al. 2014]. A rod of a given length is clamped in such a way that its tangent coincides with the gravity. Depending on the rod's geometry and its material properties, one observes that the deformed shape either remains in a plane or goes 3D, the **Bend-Twist** transition separating these two behaviours.



Fig. 23. **Bend-Twist** transition. (Left) 3D rod, with $L = 9.6$ cm. (Right) 2D rod, with $L = 9$ cm.

For this test, we fabricate our own helical rod as described in section 4.1. The moulding cylinder had a diameter of 3 cm. The coiled tube, where VPS was injected, had an interior diameter of 3.6 mm and a wall thickness of 0.75 mm. From these values, we estimate the radius and the pitch of the helical shape to be $R = 1.75$ cm and $p = 5.1$ mm, equivalent to a curvature $\kappa = 57.02 \text{ m}^{-1}$ and a torsion $\tau = 2.65 \text{ m}^{-1}$. This small intrinsic torsion is an imperfection in our setup, but the 2D/3D transition is evident as you increase the length of the rod. We show this transition in Figure 23, which happens between $L = 9$ cm and $L = 9.6$ cm.

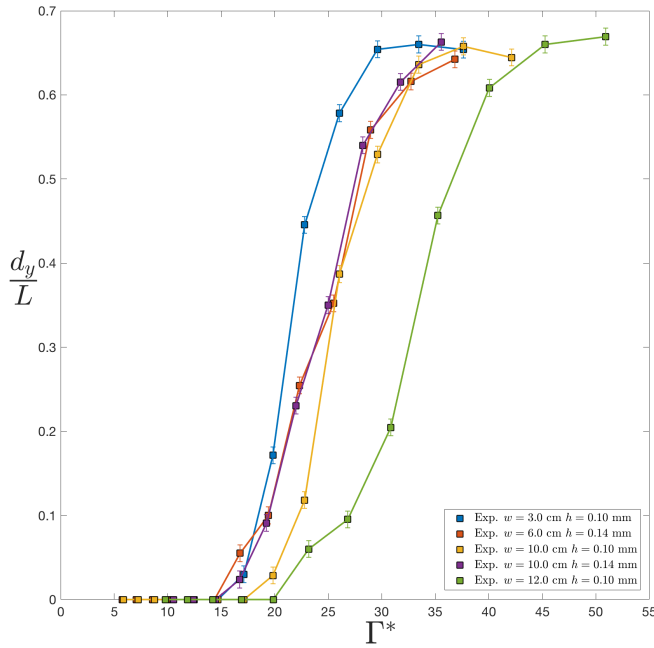


Fig. 24. Raw data **Lateral Buckling** test

The **Lateral Buckling** setup is shown in Figure 26c. This experiment is complex because the plate undergoes a large 3D deformation. To avoid time consuming digital reconstructions, we measure directly the lateral displacement of the centerline. To this end, we find the clamp projection to a position on the floor of the experimental setup. Once the plate has settled on its equilibrium shape, we gently

approach a square cross-section beam to project to the floor the position of the centerline at the free end. Finally, we measure with two orthogonal rulers the lateral displacement. The procedure is repeated for different free lengths L to sample Γ^* values. In Figure 24, we present our measurements for plates of polyethylene terephthalate (PET) of different widths w and thicknesses h .

The **Stick-Slip** setup, shown in Figure 26d, is a complex experimental setup, where we quasi-statically impose the vertical displacement of the clamp whilst measuring the lateral and normal forces. We use two calibrated Futek load cells and the force signal is digitalised with a National Instrument DAQ USB-6002. The vertical displacement is characterised by small steps of 2 mm followed by a in-position force measurement. The whole experiment is composed of a descending phase to the maximum displacement that we set to $\Delta_y = 0.33L$ and an ascending phase returning to the initial configuration to make sure the sample was not deformed plastically. However the experiment is stopped prematurely if the sample slides. Each vertical displacement is captured by a camera, and the slippage process is also captured in a video. We present in Figure 25 our force measurements for different samples with large enough friction coefficients so that sliding did not occur in the $\Delta_y \in [0, 0.33]L$ range. Each force measurement is an average of 2000 points acquired during 2 seconds at 1 kHz while the clamp remains at a given position.

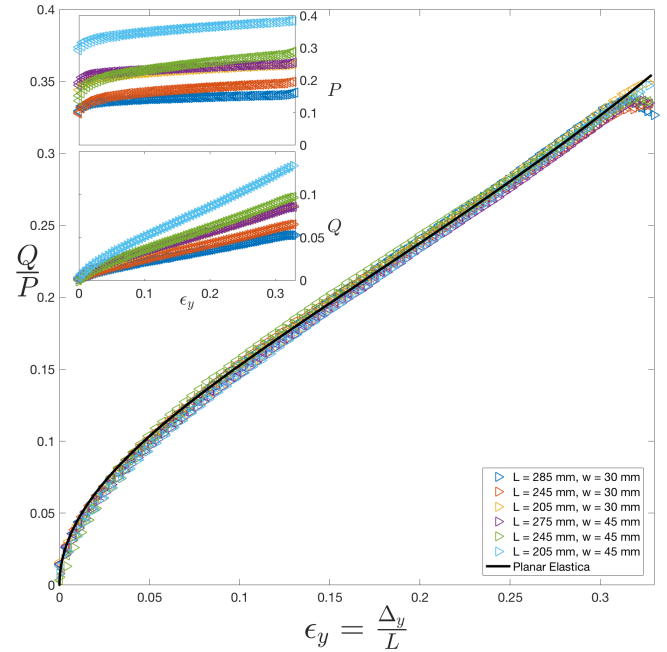


Fig. 25. Raw data **Stick-Slip** test

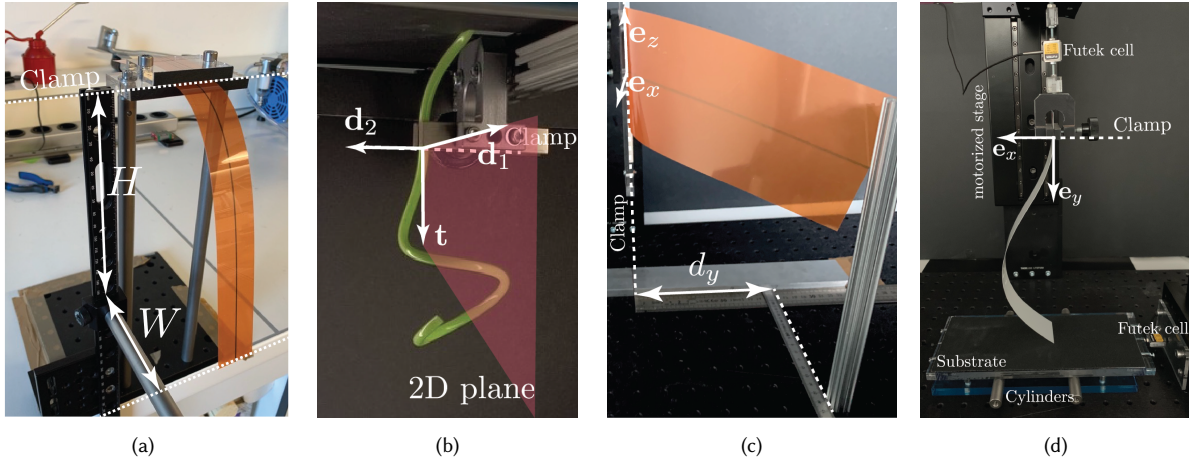


Fig. 26. Our experimental setups for the four validation tests **Cantilever** (a), **Bend-Twist** (b), **Lateral Buckling** (c), and **Stick-Slip** (d).

5 ROTATION EXPERIMENT BEHIND THE LATERAL BUCKLING TEST

5.1 Description

We present here a modification of the **Lateral Buckling** test. The clamped orientation is now tilted by an angle α from the vertical direction. The case $\alpha = 0$ corresponds to the classic **Lateral Buckling** geometry, and the case $\alpha = \pi/2$ corresponding to the **Cantilever** geometry. We let the plate hang and sag under its own weight and record the lateral displacement as α is varied from $\pi/2$ down to 0.

We have performed experiments with the same Poly-Styrene plates as in the main text, thickness $h = 0.10$ mm, density $\rho = 1410$ kg/m³, Young's modulus $E/(1 - \nu^2) \approx 7.75$ GPa, and Poisson's ratio $\nu = 0.35$. The width is here fixed to $w = 10$ cm, and three different lengths have been used $L = 17, 23$, and 27 cm, corresponding to $\Gamma^* \approx 10.52, 26.05$, and 42.14 respectively.

In addition we have simulated this new setup with the following codes: SUPER-RIBBON-clamped, LIBSHELL (STV-K/MIDEDGE/TAN), ©ABAQUS, and FENICSSHELL.

5.2 Results and analysis

The classic **Lateral Buckling** test was a bifurcation test with a binary output: either 2D or 3D solution. Here in contrast we record the continuous value of the lateral displacement as α is varied. We see that for the case $L = 17$ cm the lateral displacement is zero when $\alpha = 0$, i.e. this case lies in the 2D region of the phase diagram (Figure 4 of the Paper), far from the threshold curve. For this case all numerical codes agree fairly well with experiments. The same agreement is found for the case $L = 27$ cm where the lateral displacement at $\alpha = 0$ is clearly non zero, as this case is deep in the 3D region of the phase diagram. The case $L = 23$ cm, which is nearer to the threshold curve, is more demanding and we see that the agreement between experiments and numerics is here not uniform. Indeed, for large α all curves agree very well, but when α becomes small and approaches zero, the curves show a divergence. Here the lateral displacement quickly drops to a non-zero value, as $L = 23$ cm is indeed in the 3D region of the phase diagram, but the different axis intercepts do not agree, the experimental one being much larger than the numerical ones. This mismatch is typical of

pitchfork bifurcations which are altered by imperfections, present in experiments and not taken into account in the tested numerical codes.

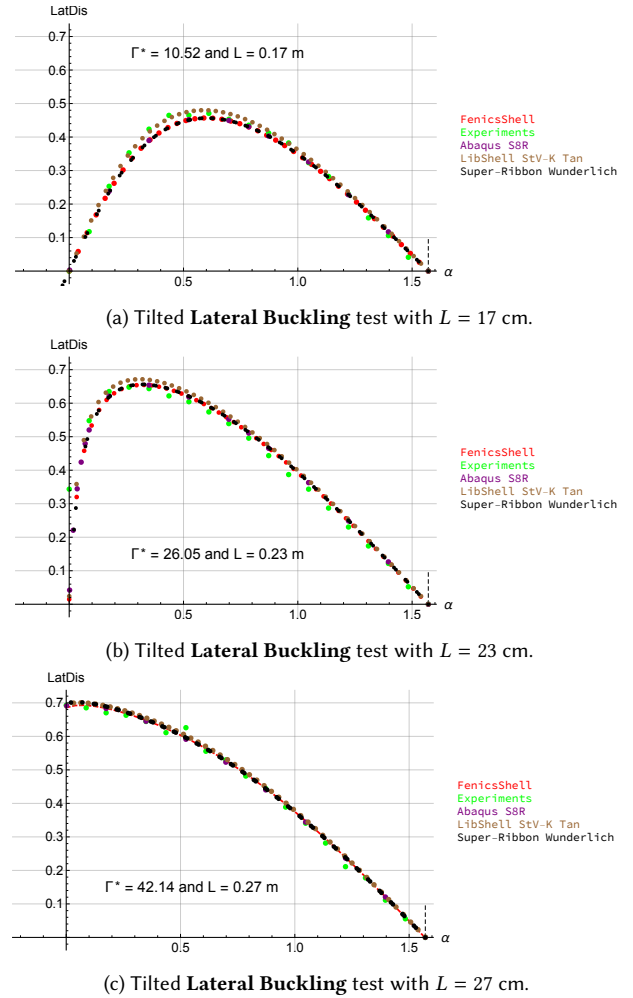


Fig. 27. Rotations experiments for the **Lateral Buckling** test.

6 FULL RESULTS ON THE CANTILEVER TEST

Here we added a **OK** score for variants that almost pass the test. This intermediary score does not need to be used in the Paper since for each test, we always obtained either one clear success or only clear failures among the different variants of the same code.



Fig. 28. Full results on the **Cantilever** test. NH stands for Neo-Hookean.

7 SOME MORE INFORMATION ON THE CODES USED

For each of the different codes used in our four tests, we list in Table 1 some aspects that were used. Please note that we do not list *general* features of the codes, but the actual setups that we used in present study.

REFERENCES

- B. Audoly and Y. Pomeau. 2010. *Elasticity and Geometry: From Hair Curls to the Non-linear Response of Shells*. Oxford University Press.
- M. Bergou, B. Audoly, E. Vouga, M. Wardetzky, and E. Grinspun. 2010. Discrete Viscous Threads. *ACM Transactions on Graphics (Proc. ACM SIGGRAPH'10)* 29, 4 (2010). <http://www.cs.columbia.edu/cg/threads>
- F. Bertails, B. Audoly, M.-P. Cani, B. Querleux, F. Leroy, and J.-L. Lévêque. 2006. Super-Helices for Predicting the Dynamics of Natural Hair. *ACM Transactions on Graphics (Proc. ACM SIGGRAPH'06)* 25 (2006), 1180–1187. Issue 3. <https://doi.org/10.1145/1141911.1142012>
- S. Bouaziz, S. Martin, T. Liu, L. Kavan, and M. Pauly. 2014. Projective Dynamics: Fusing Constraint Projections for Fast Simulation. *ACM Trans. Graph.* 33, 4, Article 154 (July 2014), 11 pages.
- R. Bridson, R. Fedkiw, and R. Anderson. 2002. Robust treatment of collisions, contact and friction for cloth animation. *ACM Trans. Graph.* 21, 3 (2002), 594–603. <http://www.cs.ubc.ca/~rbridson/docs/cloth2002.pdf>
- R. Bridson, S. Marino, and R. Fedkiw. 2003. Simulation of Clothing with Folds and Wrinkles. In *Proceedings of the 2003 ACM SIGGRAPH/Eurographics Symposium on Computer Animation (SCA '03)*. 28–36. <http://dl.acm.org/citation.cfm?id=846276.846281>
- R. Casati and F. Bertails-Descoubes. 2013. Super Space Clothoids. *ACM Transactions on Graphics (Proc. ACM SIGGRAPH'13)* 32, 4, Article 48 (July 2013), 12 pages. <https://doi.org/10.1145/2461912.2461962> <http://www.inrialpes.fr/bipop/people/casati/research.html#ssc>
- R. Charrondière, F. Bertails-Descoubes, S. Neukirch, and V. Romero. 2020. Numerical modeling of inextensible elastic ribbons with curvature-based elements. *Computer Methods in Applied Mechanics and Engineering* 364 (2020), 112922. <https://doi.org/10.1016/j.cma.2020.112922>
- H.-Y. Chen, A. Sastry, W. van Rees, and E. Vouga. 2018. Physical Simulation of Environmentally Induced Thin Shell Deformation. *ACM Trans. Graph.* 37, 4, Article 146 (July 2018), 13 pages. <https://doi.org/10.1145/3197517.3201395>
- G. Daviet, F. Bertails-Descoubes, and L. Boissieux. 2011. A Hybrid Iterative Solver for Robustly Capturing Coulomb Friction in Hair Dynamics. *ACM Trans. Graph.* 30, 6 (Dec. 2011), 1–12.
- E. Grinspun, A. Hirani, M. Desbrun, and P. Schröder. 2003. Discrete Shells. In *ACM SIGGRAPH - EG Symposium on Computer Animation (SCA'03)*. ACM-EG SCA, 62–67. <http://www.multires.caltech.edu/pubs/ds.pdf>
- J. S. Hale, M. Brunetti, S. Bordas, and C. Maurini. 2018. Simple and extensible plate and shell finite element models through automatic code generation tools. *Computers & Structures* 209 (2018), 163–181.
- D. Harmon, E. Vouga, R. Tamstorf, and E. Grinspun. 2008. Robust Treatment of Simultaneous Collisions. *ACM Trans. Graph.* 27, 3, Article 23 (Aug. 2008), 4 pages. <https://doi.org/10.1145/1360612.1360622>
- J. Li, G. Daviet, R. Narain, F. Bertails-Descoubes, M. Overby, G. Brown, and L. Boissieux. 2018. An Implicit Frictional Contact Solver for Adaptive Cloth Simulation. *ACM Trans. Graph.* 37, 4, Article 52 (Aug. 2018), 15 pages.
- M. Ly, J. Jouve, L. Boissieux, and F. Bertails-Descoubes. 2020. Projective Dynamics with Dry Frictional Contact. *ACM Transactions on Graphics* 39, 4 (2020), 1–8. <https://doi.org/10.1145/3386569.3392396>
- J. Miller, A. Lazarus, B. Audoly, and P. Reis. 2014. Shapes of a Suspended Curly Hair. *Physical Review Letters* 112, 6 (2014).
- R. Narain, A. Samii, and J. O'Brien. 2012. Adaptive Anisotropic Remeshing for Cloth Simulation. *ACM Trans. Graph.* 31, 6, Article 152 (Nov. 2012), 10 pages.
- Rasmus Tamstorf and Eitan Grinspun. 2013. Discrete Bending Forces and Their Jacobians. 75, 6 (Nov. 2013), 362–370. <https://doi.org/10.1016/j.jgmod.2013.07.001>
- H. Wang, R. Ramamoorthi, and J. O'Brien. 2011. Data-driven elastic models for cloth: modeling and measurement. *ACM Trans. Graph.* 30, 4, Article 71 (Aug. 2011), 12 pages.

Table 1. Codes configurations used in the *present* study. *some of the plots of Figure 28 were generated with a fixed mesh, see details in the captions of Figure 28.

Tested code	parameter dimensions	static / dynamic	adaptative grid or mesh
Rod			
DISCRETE ELASTIC ROD [Bergou et al. 2010]	dim	dyn	no
SUPER-HELIX [Bertails et al. 2006]	dim-less	dyn	no
SUPER-CLOTHOID [Casati and Bertails-Descoubes 2013]	dim-less	stat	no
Ribbon			
SUPER-RIBBON [Charrondière et al. 2020].	dim-less	stat	no
Plate			
LIBSHELL [Chen et al. 2018]	dim	stat	no
DISCRETE SHELL (+ LIBSHELL) [Grinspun et al. 2003]	dim	dyn	no
ARCSIM [Narain et al. 2012]	dim	dyn	yes*
DISCRETE SHELL + ARCSIM (tentative fix of ARCSIM)	dim	dyn	yes*
PROJECTIVE DYNAMICS [Bouaziz et al. 2014]	dim	dyn	no
Contact & friction			
VISCOUS FRICTION (+ SUPER-HELIX 2D)	dim	dyn	no
So-BOGUS [Daviet et al. 2011] (+ SUPER-HELIX 2D)	dim	dyn	no
ARGUS (\approx ARCSIM + So-BOGUS) [Li et al. 2018]	dim	dyn	yes
ARGUS NON ADAPTIVE (fix of ARGUS)	dim	dyn	no
BRIDSON-HARMON [Bridson et al. 2002; Harmon et al. 2008] (+ ARCSIM)	dim	dyn	no
PROJECTIVE FRICTION [Ly et al. 2020]	dim	dyn	no
Reference codes in Mechanical Engineering			
FENICSHELL [Hale et al. 2018]	dim-less	stat	no
©ABAQUS	dim	stat & dyn	yes